Catalysis Letters, Vol. 113, Nos. 3–4, February 2007 (© 2007)
DOI: 10.1007/s10562-007-9017-9

Effect of the calcium on the textural, structural and catalytic properties of $La_{1-x}Ca_xCo_{1-y}Fe_yO_3$ perovskites

Nora A. Merino,[a] Bibiana P. Barbero,[a] Caroline Cellier,[b] Julio Andrade Gamboa,[c] and Luis E. Cadús[a,*]

[a]*Instituto de Investigaciones en Tecnología Química (INTEQUI), UNSL-CONICET, Casilla de Correo 290, 5700 San Luis, Argentina*
[b]*Université Catholique de Louvain, Place Croix du Sud 2, Boite 17, 1348 Louvain la Neuve, Belgium*
[c]*CNEA, Comisión Nacional de Energía Atómica, 8400 San Carlos de Bariloche, Río Negro, Argentina*

Received 5 November 2006; accepted 20 December 2006

In $La_{1-x}Ca_xCo_{1-y}Fe_yO_3$ perovskites, the calcium substitution modifies the crystalline structure toward a pseudocubic one and produces an electronic unbalance, compensated by the formation of oxygen vacancies and Fe^{4+} ions. It also increases slightly the ethanol conversion in total combustion, compensating the detriment of catalytic activity caused by the iron substitution and it increases notably the selectivity to total oxidation.

KEY WORDS: lanthanum cobalt iron perovskite; calcium; XRD; XPS; DRIFT; Raman spectroscopy; TPR; ethanol combustion.

1. Introduction

Perovskite-type oxides have been studied due to their excellent catalytic, electronic and magnetic properties, which make them appropriate solids to be used in catalysis, in replacement of those catalysts containing noble metals. In these oxides of general formula $A_{1-x}A'_xB_{1-y}B'_yO_{3\pm\lambda}$, A is usually a lanthanide ion substituted with an alkaline earth cation (Ca, Sr, Ba) and B and B′ are transition metal ions.

Within this type of structure, the $LaCoO_3$ perovskite is one of the most studied phases as catalyst in oxidation reactions [1–5], especially those concerning pollution abatement [4–6]. Moreover, a wide range of cations has been used to substitute both the A-site and B-site (La and Co, respectively) to modify the valence of B cation, redox properties, crystalline structure and non-stoichiometry, and to control the oxygen vacancies and oxygen storage capacity. The changes of these factors are of a great importance because they are directly related to the catalytic performance.

It is known that the substitution of the A-site cation improves the oxygen ion mobility and the reducibility of the cation at B-site. In literature, other cations different from Ca, commonly Sr and Ce, at A′-site in $La_{1-x}A'_xCoO_3$ [7–9], $La_{1-x}A'_xMnO_3$ [1,7,10] and $La_{1-x}A'_xFeO_3$ [11,12] perovskites have been used to enhance the catalytic combustion reaction of several volatile organic compounds. In a previous work [13], with the aim of improving the catalytic performance in propane combustion, $LaCoO_3$ perovskite was synthesized by the citrate method and the cation at A-site was partially replaced by Ca^{2+}, resulting in $La_{1-x}Ca_xCoO_3$ oxides. It was observed that the bivalent cation modifies slightly the rhombohedral structure of the unsubstituted perovskites and generates oxygen vacancies to preserved the charge neutrality.

In addition to this, several studies substituting B-site ion have been made [11,14]. The replacement of B cation can lead to enhance catalytic activity caused by the facility of the redox process between B^{4+} and B^{3+} and a possible stabilization of the structure. It has been reported that the partial substitution of Fe for B cation in $LaB_{1-y}Fe_yO_3$ perovskites (B = Ni, Co) [15–18] increases the stability of the structure. We have reported [17] the catalytic behavior of $LaCo_{1-y}Fe_yO_3$ perovskites in the oxidation reactions of propane and ethanol as molecule models of VOCs. The $LaCoO_3$ structure can tolerate the iron inclusion with the consequent expansion of the unit cell volume, due to the higher size of the substituting cation (Fe) and preserving the rhombohedral symmetry with a weakening of B–O bonds. The capacity of the iron would be to preserve the host perovskite structure. And this effect would be related to its capacity to activate or inhibit oxidant or reducing species. Furthermore, it probably affects the capacity and the mechanism of oxygen supply or the redox behavior. The Fe^{4+} appearance would modify the redox ion couple responsible for the control of the electronic mobility in the perovskite [17,19].

The study of perovskites-type oxides with a double cationic substitution is important to take advantage of the benefits found in the substitution of each cation separately. This study requires exploring the resulting textural and chemical changes, i.e., modifications of the

*To whom correspondence should be addressed.
E-mail: lcadus@unsl.edu.ar

surface area, structure, surface composition, redox properties, and thus, how the catalytic performance is affected.

In this work, we study the effect of the partial substitution with calcium and iron in $La_{1-x}Ca_xCo_{1-y}Fe_yO_3$ perovskites on the textural properties, the structural stability and the catalytic performance for total oxidation of ethanol.

2. Experimental

2.1. Synthesis of the catalysts

$La_{1-x}Ca_xCo_{1-y}Fe_yO_3$ ($x = 0$, 0.2, 0.4; $y = 0$, 0.1, 0.3, 0.5) perovskites were prepared by the citrate method [20]. $La(NO_3)_3{\cdot}6H_2O$ (Fluka 99%), $Ca(NO_3)_2{\cdot}4H_2O$ (Sigma 99%), $Co(NO_3)_2{\cdot}6H_2O$ (Acros Organics 99%), $Fe(NO_3)_3{\cdot}9H_2O$ (Aldrich 98%) and citric acid (Merck 99.5%) were used as reagents. An aqueous solution of citric acid with a 10% excess over the number of ionic equivalents of cations was prepared. The aqueous solutions of metal nitrates were added to that of the citric acid and they were agitated for 15 min. The resulting solution was concentrated by evaporating slowly water under vacuum in a rotavapor at 75 °C until a gel was obtained. This gel was dried in an oven, increasing slowly the temperature up to 200 °C and keeping on it overnight, in order to produce a solid amorphous citrate precursor. The resulting precursor was crushed and then calcined in air at 700 °C for 2 h.

2.2. Catalyst characterization

2.2.1. BET specific surface area measurements (SSA)

The specific surface area (SSA) of the catalysts was measured by the BET method from the nitrogen adsorption isotherms obtained at 77 K on 200 mg of samples outgassed at 250 °C using a Micromeritics ASAP 2000 apparatus.

2.2.2. X-ray diffraction (XRD)

X-ray diffraction patterns of the precursors were obtained after exposing the sample at different temperatures (from room temperature to 700 °C with intervals of 50 °C) for 1 h. A Siemens diffractometer operated at 40 kV and 40 mA by employing a monochromator and Cu Kα radiation ($\lambda = 0.15418$ nm) was used. The data were collected at 0.02° with a counting time of 2 s per step, in the 2θ range of 20–90°.

X-ray diffraction patterns of the catalysts calcined at 700 °C were recorded at room temperature using a Rigaku diffractometer operated at 30 kV and 20 mA, employing Ni-filtered Cu Kα radiation ($\lambda = 0.15418$ nm). The data were collected at 0.02° with a counting time of 5 s per step, in the 2θ range of 20–90°.

In both cases, the crystalline phases were identified by reference to the powder diffraction data (PDF) employing standard spectra software.

The lattice parameters and the structure of catalysts have been estimated from Rietveld's powder structure refinement analysis [21].

2.2.3. Mössbauer spectroscopy

Mössbauer spectra at 298 and 22 K were taken in transmission geometry with a 512-channel constant acceleration spectrometer. A source of ^{57}Co in an Rh matrix of nominally 50 mCi was used. Velocity calibration was performed against a 12 μm-thick α-Fe foil. All isomer shifts (δ) mentioned in this paper are referred to this standard at room temperature. The temperature between 22 and 298 K was varied using a Displex DE-202 closed cycle cryogenic system. The spectra were folded to minimize geometric effects and were evaluated using a commercial computer fitting program named Recoil.

2.2.4. Laser raman spectroscopy (LRS)

Raman measurements were performed with a LabRam spectrometer (Dilor) interfaced with an Olympus optical microscope. The excitation radiation was a He–Ne laser (632.8 nm) operated at a power of 10 mW. The 10 × objective of the microscope was used so that a spot of about 20 μm^2 at the surface of the sample was measured at once. Spectra were obtained by averaging six scans of the Raman shift range between 1100 and 100 cm^{-1} recorded in 10 s with a spectral resolution of 7 cm^{-1}.

2.2.5. Diffuse reflectance infrared Fourier transform spectroscopy (DRIFTS)

Diffuse reflectance infrared Fourier transform (DRIFT) spectra were collected with an EQUINOX55 infrared spectrometer from Brüker equipped with cooled-air MIR source with KBr optics and a MCT detector. The samples were placed inside an environmental temperature-controlled chamber (Spectra-Tech 0030-103) equipped with SeZn windows and attached to a diffuse reflectance accessory (Spectra-Tech collector). The spectrum of an aluminum mirror was used as background. All of the spectra (between 200 and 800 scans with a 4 cm^{-1} resolution) were recorded in air or helium atmosphere (after flushing helium for 1 h) at room temperature or at 250 °C (after 30 min at this temperature). The helium flow was passed through a water trap (Gas purifier, Alltech) before being admitted into the analysis cell. The spectra are presented in absorbance mode without any manipulation.

2.2.6. X-ray photoelectron spectroscopy (XPS)

X-ray photoelectron spectroscopy analyses were performed on a Surface Science Instrument SSX 100/206 photoelectron spectrometer with a monochroma-

tized microfocused Al X-ray source. Spectra were registered after degassing at room temperature overnight and the residual pressure in the analyzer chamber was around 10^{-6} Pa. The flood gun energy was adjusted to 10 eV. The following spectra were recorded: survey spectrum, C_{1s}, O_{1s}, La_{3d}, Co_{2p}, Fe_{2p}, Ca_{2p} and again C_{1s} to check the stability of charge compensation in function of time. The data treatment was performed with the CasaXPS program (Casa Software Ltd, UK). Binding energies were calibrated with respect to the *C*–(C,H) component of C_{1s} peak fixed at 284.8 eV. The atomic ratios were calculated by using the atomic sensitivity factors provided by the manufacturer. Peak deconvolution was performed with the least squares best fitting routine included in the software after a nonlinear background subtraction, assuming an 85/15 Gaussian/Lorentzian product function.

2.2.7. Temperature-programmed reduction (TPR)

Temperature-programmed reduction experiments were performed in a quartz reactor using a thermal conductivity detector. In these experiments, 50-mg samples were pre-treated with helium gas increasing the temperature from room temperature to 700 °C at a rate of 10 °C min^{-1} and then, cooled to 50 °C. The reducing atmosphere was a 5% H_2/N_2 mixture at a total flow rate of 30 mL min^{-1}. The temperature was increased at a rate of 10 °C min^{-1} from 50 °C to 700 °C.

2.3. Catalytic test

The catalysts (300 mg, 0.5–0.8 mm particle diameter) diluted with glass particles of the same size in a ratio 1:5 were tested in a fixed bed quartz tubular reactor operated at atmospheric pressure. The feed was a C_2H_5OH:O_2:He mixture of 1:20.8:78.2. The total flow rate was 100 mL min^{-1} measured at room temperature. The temperature, measured with a coaxial thermocouple, varied from 70 °C to 325 °C in steps of 10 °C or 5 °C. The data obtained at each temperature were the average of at least three steady-state measurements. The reactants and reaction products were alternately analyzed on-line by a gas chromatograph equipped with a TCD as detector. The conversion of ethanol, *X*%, was defined as the percentage of ethanol feed that has reacted, i.e.,

$$X\% = \frac{(\text{ethanol})_{\text{in}} - (\text{ethanol})_{\text{out}}}{(\text{ethanol})_{\text{in}}} * 100$$

3. Results

3.1. Specific surface area (SSA)

The SSAs of $La_{1-x}Ca_xCo_{1-y}Fe_yO_3$ (x = 0, 0.2, 0.4; y = 0, 0.1, 0.3, 0.5, 1) catalysts, measured before and after catalytic test, are shown in table 1. The SSAs are within 10 and 18 m^2 g^{-1}. The substitution of Ca for La increases the surface area regardless of the iron levels. After the catalytic test, the SSAs vary between 2 and 3 m^2 g^{-1} for low iron content and around 1 m^2 g^{-1} for y = 0.3 and y = 0.5. The confidence interval for all the measurements is 90%. Each sample was measured at least three times, so the statistical error is strongly diminished.

3.2. X-ray diffraction (XRD)

X-ray diffraction patterns of the precursors measured at increasing temperatures indicate the crystallinity evolution as a function of calcination temperature. As we previously reported for $La_{1-x}Ca_xCoO_3$ and $LaCo_{1-y}Fe_yO_3$ [13,17], the diffractogram at room temperature reveals that the precursor was completely amorphous. The formation process of the perovskite phase starts at 550 °C. At higher temperatures, an increase of the diffraction line intensity is observed.

X-ray diffraction results of the catalysts calcined at 700 °C (figure 1) reveal the formation of perovskite-type single phases (PDF 53-1211 $LaCo_{0.5}Fe_{0.5}O_3$ and 25-1060 $LaCoO_3$). The diffractograms of the samples without calcium ($LaCo_{1-y}Fe_yO_3$ perovskites) exhibit a doublet at around $2\theta = 33$–$33.3°$, characteristic of rhombohedral symmetry. In the calcium-substituted samples, this doublet changes to a single line as well as the doublets at 2θ = 40.7–41.4, 53.4–53.9, 59.0–59.8, 69.0–69.9, 74.3–75.2, 78.8–79.5°. Furthermore, a shift of the XRD lines to higher 2θ-angle values when calcium amount increases is observed. This shift is higher for those samples with a higher iron content.

Results of structural refinement by the Rietveld method are shown in table 2. Lattice parameter a increases slightly with the increase of the calcium amount when y = 0.1, but it decreases notably when y = 0.3 and 0.5. For all of iron substitution levels, the angle α and the unit cell volume decrease when the calcium amount increases. La and Ca occupancies agree with the nominal stoichiometry for x = 0.2. For x = 0.4 with y = 0.3, 0.5, calcium does not seem to be totally included in the structure, and the stoichiometry is $La_{0.7}Ca_{0.3}$.

The oxygen occupancy decreases with the calcium amount. This decrease is more notable for low iron amounts (y = 0.1).

3.3. Mössbauer spectroscopy

Table 3 shows the hyperfine parameters. The analysis of the system is very complex since the great number of possible Fe neighbor combinations. The procedure followed is the one proposed by Russo *et al.* [22]. With all possible combinations, the corresponding probabilities for each pair (La–Ca, Co–Fe) are obtained. The hyperfine parameters are calculated and weighed by the population. The results generate 12 possible sites that

Table 1
Results of SSA ($m^2\ g^{-1}$) of $La_{1-x}Ca_xCo_{1-y}Fe_yO_3$ perovskites ($x = 0, 0.2, 0.4$; $y = 0.1, 0.3, 0.5$) calcined at 700 °C before and after catalytic test, reaction temperature at 50% of ethanol conversion (T_{50}) and at 90% of CO_2 yield (T_{90}), feeding a $C_2H_5OH:O_2$:He mixture of 1:20.8:78.2 with a total flow rate of 100 mL min^{-1} and operating at atmospheric pressure

y	x	SSA ($m^2\ g^{-1}$)		T_{50} (°C)	T_{90} (°C)
		Fresh	Used		
0	0	7.3[a]	9.2[a]	–	249
	0.2	13.6[a]	15.7[a]	–	245
	0.4	14.4[a]	19.3[a]	–	234
0.1	0	10.9	8.0	196	243
	0.2	18.1	15.3	194	233
	0.4	13.1	14.1	195	235
0.3	0	14.3	13.9	205	256
	0.2	18.3	18.1	192	233
	0.4	16.0	16.8	192	230
0.5	0	9.6	8.9	205	251
	0.2	11.8	13.1	200	239
	0.4	13.7	15.1	201	239
1	0	18.5[b]	12.8[b]	257	–
	0.2	13.0[b]	9.7	245	–
	0.4	16.7[b]	15.3	237	–

[a] From Ref. [13].
[b] From Ref. [19].

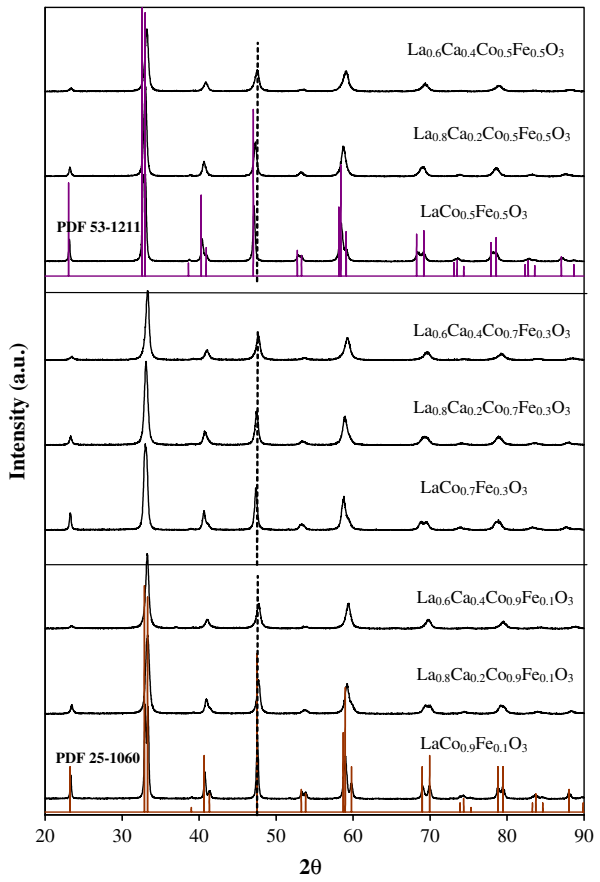

Figure 1. XRD profiles at room temperature of fresh $La_{1-x}Ca_xCo_{1-y}Fe_yO_3$ perovskites ($x = 0, 0.2, 0.4$; $y = 0.1, 0.3, 0.5$) calcined at 700 °C during 2 h.

are divided in groups of 4, based on the similarity of the magnetic hyperfine fields. After recalculating the parameters, they are fixed and only the areas are allowed to change. A signal at 509 kG was discarded due to its low value and the one at 464 kG is assigned to a non-Gaussian distribution because of the appearance of asymmetric lines. Also, a central doublet is used and due to its low δ it could be ascribed to Fe^{4+} instead of Fe^{3+}. Finally, a sextet assigned to Fe^{4+} also appears. At room temperature, only a singlet appears which is fitted with a doublet of very small quadrupolar splitting value (Δ), indicating a high symmetry in all of Fe^{3+} sites and a Fe^{4+} singlet. The estimated percentage for this last cation is $15 \pm 3\%$.

3.4. Laser Raman spectroscopy (LRS)

Raman spectra of $La_{1-x}Ca_xCo_{1-y}Fe_yO_3$ perovskites are exposed in figure 2. They show bands at 405 cm^{-1} (very strong), 450 cm^{-1} (weak), 485 cm^{-1} (medium), 590 cm^{-1} (medium), 675 cm^{-1} (very weak), 705 cm^{-1} (strong), and 815 cm^{-1} (very weak). The spectra obtained are similar to those corresponding to rhombohedral $LaFeO_3$ [19], rhombohedral $LaCoO_3$ [13] and rhombohedral $LaNiO_3$ [23]. Also, Popa *et al.* [24] obtained very similar spectra for these three perovskite phases. On the other hand, Granado *et al.* [25] assigned the 494 and 604 cm^{-1}modes to the orthorhombic $LaMnO_3$ phase. Regardless of the iron content, the intensity of the bands decreases when the calcium amount increases.

Table 2
Crystalline cell parameters and ions occupancies of fresh $La_{1-x}Ca_xCo_{1-y}Fe_yO_3$ perovskites calcined at 700 °C from the structural refinement by Rietveld method

x	y	a (Å)	α ()	V(Å^3)	Ooccupancy	Laoccupancy	Caoccupancy
0	0.1	5.386	60.7	112	0.99	1[a]	0[a]
	0.3	5.416	60.6	114	0.98	1[a]	0[a]
	0.5	5.439	60.6	115	0.99	1[a]	0[a]
0.2	0.1	5.387	60.5	112	0.97	0.84	0.16
	0.3	5.410	60.4	113	0.96	0.84	0.16
	0.5	5.436	60.3	114	0.96	0.81	0.19
0.4	0.1	5.388	60.1	111	0.88	0.62	0.38
	0.3	5.405	60.2	112	0.94	0.70	0.30
	0.5	5.426	60.2	113	0.92	0.71	0.29

[a] Without refinement.

Table 3
Hyperfine parameters of fresh $La_{0.6}Ca_{0.4}Co_{0.5}Fe_{0.5}O_3$ perovskite calcined at 700 °C, measured at 24 and 298 K

Species	T (K)	H (kG)	Δ (mm/s)	δ (mm/s)	2ε (mm/s)	%
Group 1	24	529	–	0.44	−0.05	20 ± 2
Group 2	24	489	–	0.47	−0.09	24 ± 3
Group 3	24	445	–	0.46	−0.11	42 ± 3
Fe^{4+}	24	261 ± 8	–	−0.1 ± 0.1	0.1 ± 0.1	9 ± 2
Paramagnetic and/or supermagnetic Fe^{3+}	24	–	–	0.16 ± 0.09	–	6 ± 1
Fe^{3+}	298	–	0.4 ± 0.1	0.4 ± 0.1	–	78 ± 23
Fe^{4+}	298	–	–	0.1 ± 0.1	–	22 ± 23

Group 1: Fe^{3+}: Ca(0,2) + Co(0);Ca(3) + Co(0);Ca(4) + Co(0).
Group 2: Fe^{3+}: Ca(0,2) + Co(3);Ca(3) + Co(3);Ca(4) + Co(3);Ca(5) + Co(2).
Group 3: Fe^{3+}: Ca(5) + Co(3).
δ [mm/s]: isomeric shift.
Δ [mm/s]: quadrupolar splitting.
H [kG]: hyperfine field.

3.5. *Diffuse reflectance infrared Fourier transform spectroscopy (DRIFTS)*

Figure 3 shows DRIFT spectra of $La_{1-x}Ca_xCo_{1-y}Fe_yO_3$ perovskites. DRIFT spectra of $La_{0.8}Ca_{0.2}Co_{1-y}Fe_yO_3$ present a band at around 635–649 cm^{-1}. Its intensity increases with the iron content. The typical spectra of ABO_3 perovskite oxides exhibit bands at 500–730 cm^{-1} region assigned to stretching modes of BO_6 octahedra [26–28]. Bands at around 885 and 905 cm^{-1} appear in $La_{0.6}Ca_{0.4}Co_{1-y}Fe_yO_3$ perovskites and their intensity increases slightly with the iron amount. The exposure of catalysts to inert atmosphere (helium) does not modify the spectra.

3.6. *X-ray photoelectron spectroscopy (XPS)*

La3d$_{5/2}$ peak is detected at 833.5 ± 0.3 eV. According to literature [29–31], this corresponds to La^{3+}. The Ca2p peak is at 346.7 ± 0.3 eV, and it is Ca^{2+} [30]. Co2p peak has a binding energy of 779.7 eV which is characteristic of Co^{3+}. It has been reported [32] that Co^{2+} exhibits a satellite peak at 785–788 eV. None of the samples shows a satellite peak. Fe2p peak appears at 710.0–710.6 eV. This binding energy would be characteristic of Fe^{3+} [33,34]. The analysis of Fe2p peak to determine iron oxidation states other than +3 is quite difficult since it is overlapped by Co Auger signal. Binding energy shifts caused by the calcium substitution are not observed. Table 4 shows the surface atomic ratios obtained from XPS. (La + Ca)/(Co + Fe) atomic ratios are more than the double of the theoretical value. Furthermore, Ca/(La + Ca) atomic ratio is much higher than the theoretical one. This indicates a surface enrichment in La and Ca. The O1s peak is deconvoluted considering several components as described in [35]. The relative content of lattice oxygen species: O_L (O^{2-}) and adsorbed oxygen species: O_{ad} (O_2^{2-}/O^-) can be estimated from the areas of the sub-peaks. The O^{2-}/(La + Ca + Co + Fe) surface atomic ratios decrease linearly with calcium content, regardless of the iron content.

3.7. *Temperature-programmed reduction (TPR)*

The reduction curves of $La_{1-x}Ca_xCo_{1-y}Fe_yO_3$ (x = 0, 0.2, 0.4; y = 0.1, 0.5) are shown in figure 4. All of the catalysts exhibit a reduction signal starting at about 200 °C with a maximum within 350–400 °C. The calcium substitution does not appreciably affect this signal. With y = 0.1 and 0.3, a second reduction signal at high

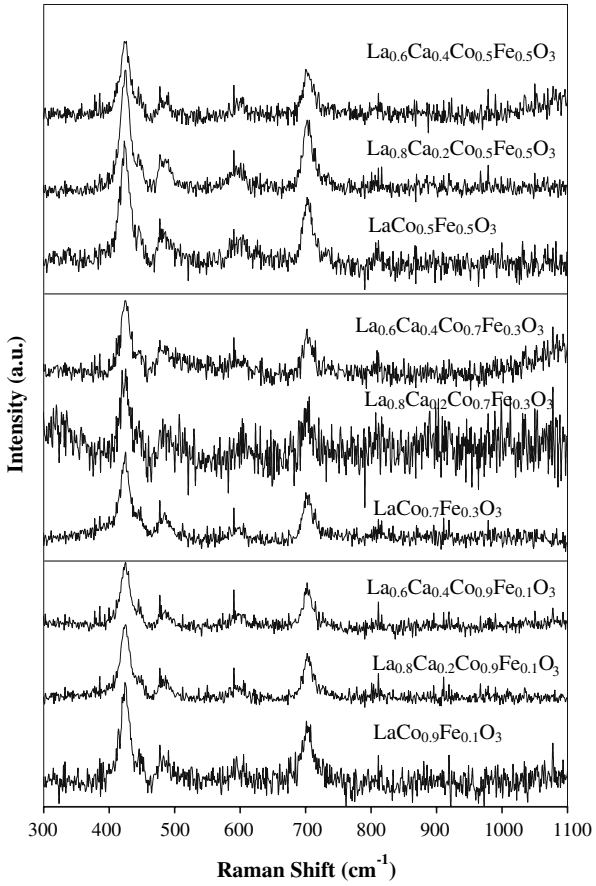

Figure 2. Raman spectra of fresh $La_{1-x}Ca_xCo_{1-y}Fe_yO_3$ perovskites (x = 0, 0.2, 0.4; y = 0.1, 0.3, 0.5).

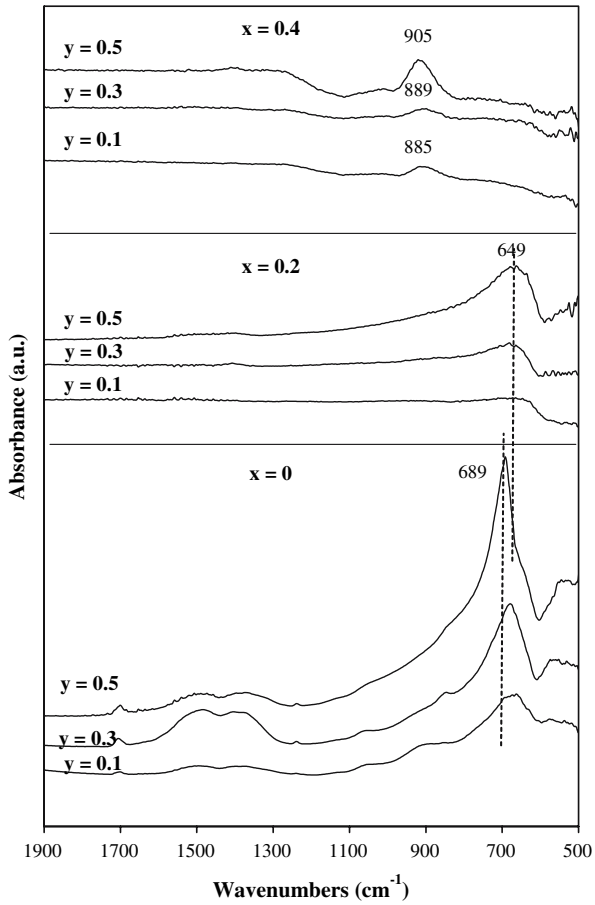

Figure 3. DRIFT spectra of fresh $La_{1-x}Ca_xCo_{1-y}Fe_yO_3$ perovskites (x = 0, 0.2, 0.4; y = 0.1, 0.3, 0.5) at room temperature in He flow during 1 h.

temperature is observed. The presence of calcium decreases the maximum temperature of this step regardless of its amount.

3.8. Catalytic activity

Table 1 shows the temperature corresponding to 50% ethanol conversion (T_{50}) and the temperature corresponding to 90% CO_2 yield (T_{90}). Figure 5 presents the selectivity to CO_2 as a function of the reaction temperatures in the ethanol oxidation reaction of $La_{1-x}Ca_xCo_{0.3}Fe_{0.3}O_3$ perovskites (x = 0, 0.2; 0.4) since all of the perovskites show the same behaviour of this serie.

These parameters are good indicators of the catalytic activity and they facilitate the comparison among the catalysts. The results of $La_{1-x}Ca_xFeO_3$ perovskites are shown as reference. The conversion is not affected by calcium substitution when y = 0.1. However, the conversion increases with calcium substitution for y = 0.3 and y = 0.5, thus, the activity detriment caused by the increase of the iron amount is compensated. At any amount of iron in the structure, the mere presence of calcium improves the yield to CO_2, i.e., the selectivity to complete oxidation reaction.

4. Discussion

4.1. Textural and structural properties

The series of $La_{1-x}Ca_xCo_{1-y}Fe_yO_3$ perovskite-type oxides was synthesized by the citrate method because this technique has shown to be very appropriate to obtain high purity perovskite oxides and relatively high SSAs in comparison with other synthesis methods [13,19,33,34]. Effectively, the surface areas resulted within 10 and 18 $m^2\ g^{-1}$ and, as it has been observed in $La_{1-x}Ca_xCoO_3$ perovskites [13], the incorporation of calcium produces an increase on the surface area regardless of the iron levels. This textural modification may be due to (i) structural defects induced by a partial substitution, or (ii) segregation of phases, if the substitution is not completely achieved.

The XRD results (figure 1) showed that the samples obtained were pure single phases. However, the detection limit of this technique does not permit to identify oxide phases at trace level that may segregate during the preparation. To determine this, spectroscopy techniques more sensible than XRD were employed. Mössbauer spectroscopy was used to detect iron oxide traces. Fe_2O_3

Table 4
Surface atomic ratios and surface oxygen vacancies of $La_{1-x}Ca_xCo_{1-y}Fe_yO_3$ from XPS

y	x	$O^{2-}/(La+Ca+-Co+Fe)$		$O_{ad}/(La+Ca+-Co+Fe)$[b]		$Ca/(La+Ca)$		$(La+Ca)/(Co+Fe)$		λ'[c]
		Fresh	Used	Fresh	Used	Fresh	Used	Fresh	Used	
0	0	1.25[a]	1.34	–	–	–	–	–	–	0.50[d]
	0.2	1.21[a]	1.02	–	–	–	–	–	–	0.58[d]
	0.4	1.08[a]	1.17	–	–	–	–	–	–	0.84[d]
0.1	0	1.50	1.39	0.68	0.82	0	0	2.00	2.00	0.0
	0.2	1.29	1.24	0.94	1.00	0.39	0.22	4.00	2.40	0.42
	0.4	1.01	1.62	0.73	0.92	0.54	0.44	2.70	2.60	0.98
0.3	0	1.28	1.35	0.88	0.93	0	0	2.30	3.00	0.44
	0.2	1.21	1.64	0.62	1.13	0.36	0.32	2.45	2.40	0.58
	0.4	1.07	1.55	0.65	1.01	0.51	0.41	2.80	2.60	0.86
0.5	0	1.71	1.37	0.72	0.73	0	0	2.20	2.20	–
	0.2	1.31	1.71	0.75	0.80	0.44	0.30	2.80	2.50	0.38
	0.4	1.11	1.43	0.62	1.09	0.61	0.38	2.90	2.30	0.78

[a] From Refs. [13,35].
[b] O_{ad}: adsorbed oxygen ($O_2^{2-}+O^-$), from Ref. [35].
[c] λ': surface oxygen vacancies calculed as $\lambda' = 3–2[O^{2-}/(La+Ca+Co+Fe)]$.
[d] From Ref. [35].

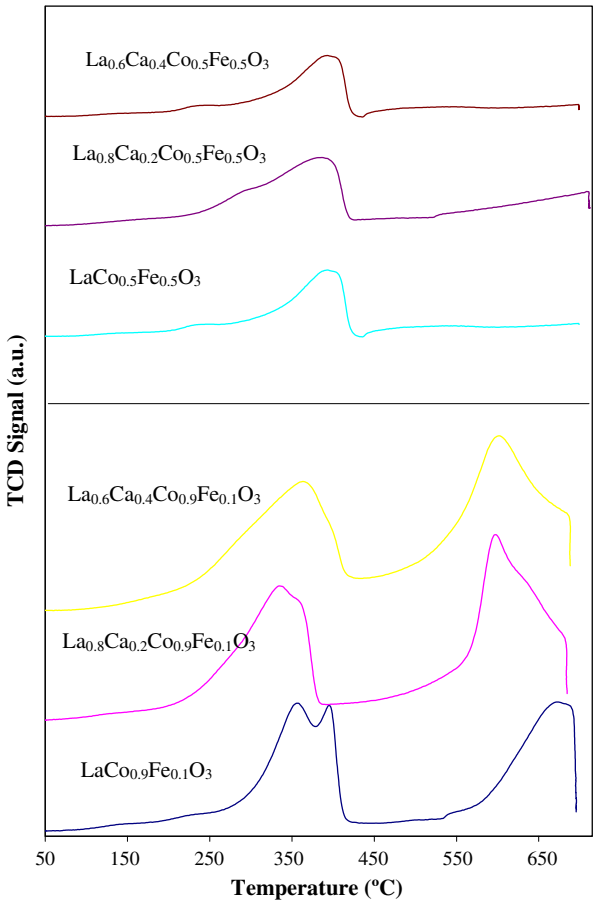

Figure 4. TPR profiles of fresh $La_{1-x}Ca_xCo_{1-y}Fe_yO_3$ perovskites (x = 0, 0.2, 0.4; y = 0.1, 0.5) calcined at 700 °C, pre-treated with He flow in a range of room temperature – 700 °C at 10 °C min^{-1} and reduced with a 5% H_2/N_2 mixture of 30 mL min^{-1} in the same temperature range.

gives a characteristic doublet easily distinguished from the perovskite spectrum [36,37]. As the perovskites spectra show no signal of Fe_2O_3, and considering the high symmetry of Fe^{3+} ions, Fe_2O_3 existence can be discarded.

The cations occupying the A-site, lanthanum and calcium, can form oxocarbonates and carbonates when they are as oxides. However, when these cations are included in a structure such as the perovskite, they are stable and the formation of carbonates is avoided. Thus, a study using DRIFT spectroscopy – a technique particularly sensible to carbonate detection – may be useful to discriminate if lanthanum and calcium were successfully incorporated in the perovskite structure. In this study, the samples were undergone different conditions (helium and air atmosphere, at room temperature and 250 °C). The DRIFT spectra of $LaCo_{1-y}Fe_yO_3$ perovskites (measured under helium or air atmosphere at room temperature) showed a doublet in the region of 1400–1600 cm^{-1} assigned to carbonated species [17]. When calcium substituted for lanthanum, carbonate signal disappeared. Thus, DRIFT results suggest that calcium substitution favors the inclusion of lanthanum ions within the perovskite structure.

Another important insight into XRD results is that there is a change of the crystalline structure. $LaCo_{1-y}Fe_yO_3$ perovskites with $y \leq 0.5$ exhibit rhombohedral structure [6,16,17]. The doublet around $2\theta = 32°$, which is characteristic of perovskites with rhombohedral structure, becomes a single peak at approximately 33°, when calcium partially substitutes for lanthanum. This change is observed with a 20% of calcium substitution. At higher substitution level (x = 0.4), peaks are narrower. Apparently, the structure changes toward a

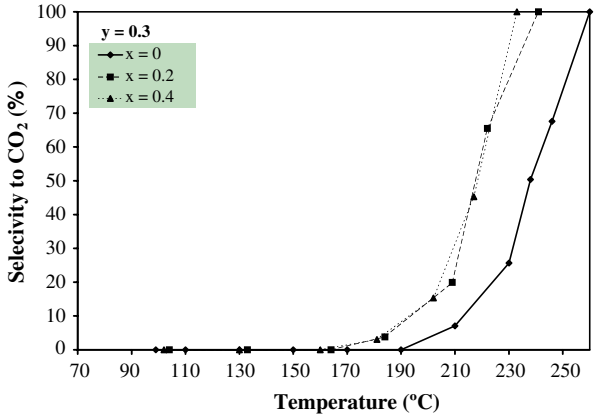

Figure 5. Selectivity to CO_2 as a function of the reaction temperatures in the ethanol oxidation reaction using 300 mg of $La_{1-x}Ca_xCo_{0.3}Fe_{0.3}O_3$ perovskites ($x = 0$, 0.2; 0.4) feeding a C_2H_5OH:O_2:He mixture of 1:20.8:78.2 with a total flow rate of 100 mL min^{-1}.

pseudocubic one. The results of structural refinement by the Rieltveld method confirm this assumption. The typical perovskite presents cubic structure, i.e., $\alpha = 60°$. The refinement of our diffractograms was made considering a rhombohedral structure. Thus, the decrease of the α-angle value with the increased calcium amount indicates a lower structure distortion, i.e., a crystalline structure tending to a cubic symmetry. A characterization technique particularly sensible to structural changes is Raman spectroscopy. The results indicate that the signal intensity decreases with the increase of the calcium content. The same was observed with $La_{1-x}Ca_xFeO_3$ perovskites [19] and assigned to a structural change toward a pseudocubic structure. Thus, the Raman spectra confirm what was suggested by the XRD results.

From the results discussed so far, a partial conclusion can be achieved. The citrate method is a very appropriate way to synthesize perovskites with relatively high SSA and good purity. Calcium substitution modifies the crystalline structure toward a pseudocubic one and it increases the SSA and the lanthanum incorporation into the perovskite structure.

4.2. Electroneutrality

The partial substitution for lanthanum (oxidation state +3) with a cation of lower valence such as calcium (+2) causes an electronic unbalance in the perovkite structure. To preserve the electroneutrality, two situations may occur: (i) an increase of the oxidation state of B cation (cobalt or iron, in our case) and/or (ii) the formation of oxygen vacancies. The nature of the B cation will lead to one or both of the previous situations. In $La_{1-x}Ca_xCoO_3$ perovskites, it was found that the charge compensation was achieved by the formation of oxygen vacancies [13]. On the other hand, in $La_{1-x}Ca_xFeO_3$ perovskites, iron increases its oxidation state to +4 and oxygen vacancies are formed only with calcium substitution levels higher than 20% [19]. To determine which situation prevails in $La_{1-x}Ca_xCo_{1-y}Fe_yO_3$ perovskites, where both situations – the increase of iron oxidation state and the formation of oxygen vacancies – may occur, results from several characterization techniques were considered.

Direct evidence about the existence of Fe^{4+} could be obtained from XPS but, unfortunately, the analysis of Fe2p peak at 710.1–710.2 eV is difficult. The decovolution of this peak to detect contributions from different iron oxidation state is very unreliable, since Co Auger signal overlaps it.

In other works about orthoferrites [19,38], the existence of Fe^{4+} was determined from indirect measurements by TPR and XRD. The reduction of Fe^{4+} to Fe^{3+} proceeds at about 250–450 °C, depending on the experimental conditions. The reduction curves of $La_{1-x}Ca_xCo_{1-y}Fe_yO_3$ perovskites (figure 4) present an intense signal with a maximum at 335–395 °C, which is mainly due to the reduction of Co^{3+} to Co^{2+}. Thus, the reduction signals of Co^{3+} and Fe^{4+}, if the latter exists, are overlapped. To determine whether the reduction signal only corresponds to Co^{3+} or the Fe^{4+} signal is also included, the hydrogen consumption that corresponds to that reduction stage was estimated calculating the area under the curve in a range of 100–450 °C. If the unbalance generated as a result of the partial substitution of Ca for La is compensated with the appearance of Fe^{4+}, the hydrogen consumption should increase with the calcium amount. To visualize this in a better way, the hydrogen consumption as a function of the iron content was drawn, considering the calcium content as a parameter (figure 6). As it is expected, the hydrogen consumption decreases when the iron content increases, since it is not reduced (under the TPR conditions used in this work) when it constitutes the perovskite structure [17,19]. The difference observed between the $x = 0$ curve and the $x = 0.2$ one makes us suppose the Fe^{4+} formation.

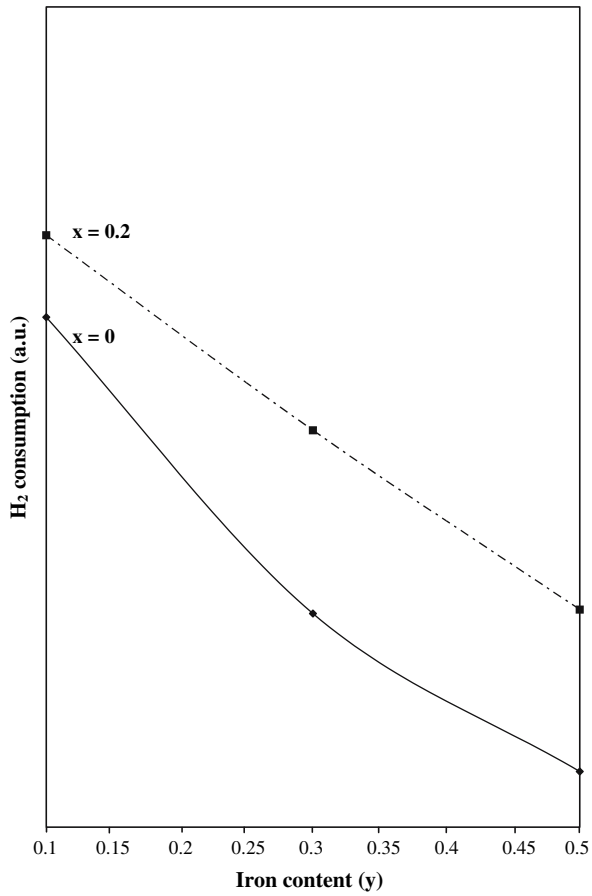

Figure 6. Hydrogen consumption from TPR results as a function of the iron content of $La_{1-x}Ca_xCo_{1-y}Fe_yO_3$ perovskites (x = 0, 0.2; y = 0.1, 0.3, 0.5).

The XRD results reveal the existence of Fe^{4+}. The peaks shift toward higher 2θ angles as the calcium amount increases indicates a smaller interplanar distance, i.e., the unit cell volume decreases. The change of the unit cell size cannot be only attributed to the difference between the ionic radii of the calcium and lanthanum, since they are quite similar (1.34 Å for Ca^{2+} and 1.36 Å for La^{3+} [39]). In contrast, the ionic radius of Fe^{4+} is significantly smaller than that of Fe^{3+} (0.585 Å for Fe^{4+} and 0.645 Å for Fe^{3+} [39]); thereby, the decrease of the unit cell volume would be caused by the existence of Fe^{4+}. The DRIFT results are in line with the XRD ones. In figure 3, it can be observed that the bands shift to lower wavenumbers. This behavior may be ascribed to a reinforcement of the metal–oxygen bonds, due to the contraction of the cell volume. Moreover, DRIFT spectra of $La_{0.6}Ca_{0.4}Co_{1-y}Fe_yO_3$ show a band at about 900 cm^{-1}. In the FT-IR spectra of $La_{1-x}Ca_xFeO_3$ perovskites, a band at 877 cm^{-1} assigned to structural modifications produced by the substitution with calcium and probably associated to the Fe^{4+} ion formation was observed [19]. Although it is difficult to analyze the Mössbauer spectra due to a great number of possible neighbors' combinations of Fe, the presence of about 15% of Fe^{4+} can be inferred from a fit following the parameters studied for $La_{0.6}Ca_{0.4}FeO_3$ (B.P. Barbero *et al.*, submitted).

The shift of the XRD peak is more notable in perovskites with higher iron amount. In the samples with only 10% of iron, probably the electronic unbalance cannot be totally compensated by the elevation of the iron oxidation state and so, another phenomenon such as oxygen vacancies formation may occur. The oxygen vacancies can be distributed in the bulk or at the surface and the concentration of such vacancies may be different in each case. The existence of oxygen vacancies in the bulk would be assumed from the results of oxygen occupancy obtained by Rietveld's method. Thus, the oxygen vacancies increase with calcium amount. The concentration of oxygen vacancies at the surface, λ', can be estimated from XPS measurement (table 4) by means of $\lambda' = 3–2[O^{2-}/(La + Ca + Co + Fe)]$ [13,40] where O^{2-} is referred to the lattice oxygen amount and the chemical symbols to the corresponding amount of each element. The results present a great dispersion but, in average, the concentration of surface oxygen vacancies clearly increases with the increase of calcium amount (figure 7).

In conclusion, the electronic unbalance caused by the calcium substitution in $La_{1-x}Ca_xCo_{1-y}Fe_yO_3$ perovskites is compensated by both the elevation of the oxidation state of the Fe ions and the generation of oxygen vacancies.

4.3. Catalytic performance and stability

The oxygen vacancies generated by calcium substitution can act as adsorption centers or can increase oxygen mobility to favor a Mars-van Krevelen mechanism at high reaction temperature. In previous studies [13,19], we reported that the substitution of calcium for lanthanum in $La_{1-x}Ca_xCoO_3$ and $La_{1-x}Ca_xFe_yO_3$ perovskites increases propane and ethanol conversion in the total oxidation reaction. In $La_{1-x}Ca_xCo_{1-y}Fe_yO_3$ perovskites, however, the effect of calcium substitution on ethanol conversion is not very important. Only a slight increase of the catalytic activity is observed when iron substitution level is higher than 10%, regardless of calcium amount. However, the conversion increases with calcium substitution for y = 0.3 and y = 0.5. Thus, the calcium substitution compensates the detriment of catalytic activity caused by the iron substitution.

It is known that ethanol oxidation proceeds by means of the formation of an intermediate, the acetaldehyde. This by-product is more harmful for human health than ethanol and so, it is necessary to avoid its production. Thereby, the important increase of the selectivity (or yield) to CO_2 (figure 5) obtained with the substituted catalysts is very beneficial and this is the more relevant effect of the incorporation of calcium in $La_{1-x}Ca_xCo_{1-y}Fe_yO_3$ perovskites.

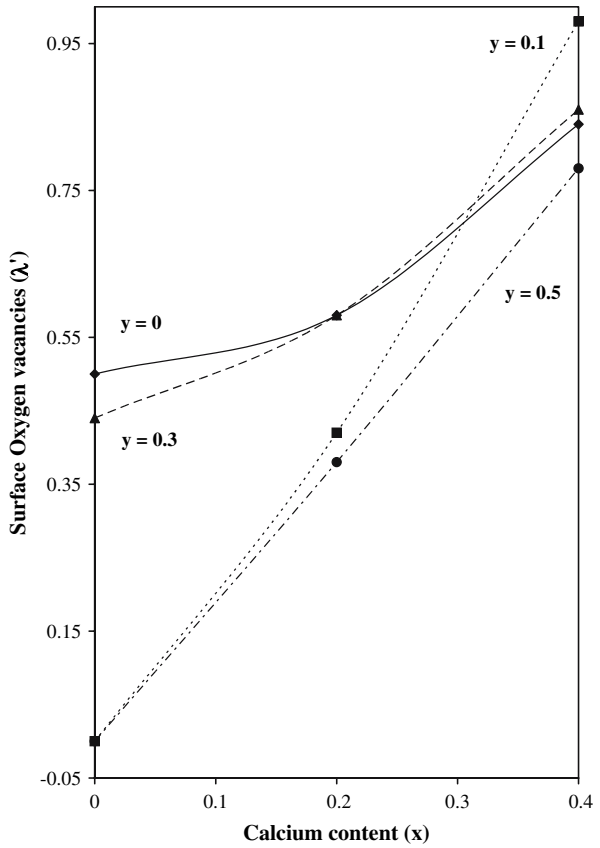

Figure 7. Surface oxygen vacancies curves as a function of the calcium content in fresh $La_{1-x}Ca_xCo_{1-y}Fe_yO_3$ perovskites ($x = 0$, 0.2, 0.4; $y = 0$, 0.1, 0.3, 0.5), calculated from XPS results as $\lambda' = 3–2$ $[O^{2-}/(La + Ca + Co + Fe)]$.

In $LaCo_{1-y}Fe_yO_3$ perovskites [17], the main effect of iron substitution is the increase of structural stability. Furthermore, at low substitution level, the catalytic performance improves even after thermal hydrotreatment. In contrast, the calcium substitution would decrease structural stability. This would be assumed from the TPR results considering the decrease of the temperature of second reduction step with calcium substitution, i.e., the presence of calcium facilitates the system reduction. The XRD results of the samples after TPR offer important evidence about the structural stability. When iron substitutes for cobalt, the perovskite structure is preserved after the TPR but when calcium substitutes for lanthanum, additional diffraction lines corresponding to La_2O_3 (PDF 5-602, 22-0369) and Co (PDF 15-806) are detected. The intensity of these last phases increases with calcium amount indicating the destabilizing effect of calcium in the perovskite structure.

If we consider the variation of the SSA of the catalyst before and after the catalytic test as an indicator of textural stability, the stabilizing effect of iron is observed. The samples with $y = 0$ and 0.1 present variations of SSAof 2–3 $m^2\ g^{-1}$ while for the samples with $y = 0.3$ and $y = 0.5$, the variation is around 1 $m^2\ g^{-1}$.

In summary, calcium substitution increases slightly ethanol conversion compensating the detriment of the catalytic activity caused by iron substitution. Thus, due to the presence of calcium in the catalyst, a higher iron amount is incorporated in order to increase the structural stability, preserving the catalyst performance. Nevertheless, the most important effect of calcium substitution is the increase of the selectivity to total oxidation limiting the yield to acetaldehyde.

5. Conclusions

The calcium substitution increases slightly ethanol conversion compensating the detriment of the catalytic activity caused by iron substitution. Thus, due to the presence of calcium in the catalyst, a higher iron amount is incorporated in order to increase the structural stability preserving the catalyst performance. Nevertheless, the most important effect of calcium substitution is the increase of the selectivity to total oxidation limiting the yield to acetaldehyde.

Calcium substitution modifies the crystalline structure toward a pseudocubic one and it increases the SSA and lanthanum incorporation into the perovskite structure. The citrate method is a very appropriate way to synthesize perovskites with relatively high SSA and good purity.

The electronic unbalance caused by the substitution of calcium (+2) for lanthanum (+3) in the perovskite is compensated by both the elevation of the oxidation state of part of the Fe ions and the generation of oxygen vacancies.

Acknowledgments

Financial support from CONICET, Universidad Nacional de San Luis, ANPCyT and SEPCyT (Argentina)-FNRS (Belgium) is gratefully acknowledged. The authors also thank Gustavo Marchetti (CINDECA, La Plata, Argentina) for the Mössbauer study and Pierre Eloy (Universite Catholique de Louvain, Louvain la Neuve, Belgium) for his help with XPS analyses.

References

[1] H. Arai, T. Yamada, K. Eguchi and T. Seiyama, Appl. Catal. 26 (1986) 265.
[2] S. Royer, H. Adamdari, D. Duprez and S. Kaliaguine, Appl. Catal. B 58 (2005) 273.
[3] M. Alifanti, N. Blangenois, M. Florea and B. Delmon, Appl. Catal. A 280 (2005) 255.
[4] M. Alifanti, M. Florea, V. Cortes-Corberon, U. Endrusehat, B. Delmon and N.I. Panvulescu, Catal. Today 112 (2006) 169.
[5] N. Yin, Y. Cao, Y. Su, W. Dai, H. He and K. Fan, J. Catal. 230 (2005) 249.

[6] M. O'Connell, A.K. Norman, C.F. Hüttermann and M.A. Morris, Catal. Today 47 (1999) 123.
[7] S. Irusta, M.R. Pina, M. Menéndez and J. Santamaría, J. Catal. 179 (1998) 400.
[8] T. Seiyama, N. Yamazoe and K. Eguchi, Ind. Eng. Chem. Prod. Res. Dev. 24 (1985) 19.
[9] N. Yamazoe, Y. Teraoka and T. Nakamura, Chem. Lett. (1981) 1767.
[10] D. Weng, H. Zhao, X. Wu, L. Xu and M. Shen, Mater. Sci. Eng. A 361 (2003) 173.
[11] M. Alifanti, J. Kirchnerova, B. Delmon and D. Klavana, Appl. Catal. A 262 (2004) 167.
[12] C.H. Wang, C.L. Chen and H.S. Weng, Chemosphere 57 (2004) 1131.
[13] N.A. Merino, B.P. Barbero, P. Grange and L.E. Cadús, J. Catal. 231 (2005) 232.
[14] P. Ciambelli, S. Cimino, S. De Rossi, L. Lisi, G. Minelli, P. Porta and G. Russo, Appl. Catal. B 29 (2001) 239.
[15] H. Tanaka, N. Mizuno and M. Misono, Appl. Catal. A 244 (2003) 371.
[16] M.R. Goldwasser, M.E. Rivas, M.L. Lugo, E. Pietri, M.J. Pérez-Zurita, M.L. Cubeiro, A. Griboval-Constant and G. Leclercq, XIX Simposio Iberoamericano de Catálisis, Mérida, Yucatán, México (2004) 78.
[17] N.A. Merino, B.P. Barbero, P. Ruiz and L.E. Cadús, J. Catal. 240 (2006) 245.
[18] H. Falcón, A.E. Goeta, G. Punte and R.E. Carbonio, J. Sol. State Chem. 133 (1997) 379.
[19] B. Barbero, J. Andrade Gamboa and L.E. CadúsAppl., Catal. B 65 (2006) 21.
[20] P. Courty, H. Ajot, C. Marcilly and B. Delmon, Power Technol. 7 (1973) 21.
[21] R.A. Young, A. Sakthivel, T.S. Moss and C.O. Paiva-SantosDBWS-9411 – an upgrade of the DBWS programs for Rietveld Refinement with PC and mainframe computers., J. Appl. Cryst. 28 (1995) 366.
[22] U. Russo, L. Nodari, M. Faticanti, V. Knucser and G. Filoti, Sol. State Ion. 176 (2005) 97.
[23] E. Bontempi, C. Garzella, S. Valetti and L.E. Depero, J. Eur. Ceram. Soc. 23 (2003) 2135.
[24] M. Popa, J. Frantti and M. Kakihana, Sol. State Ion. 154–155 (2002) 135.
[25] E. Granado, N.O. Moreno, A. García, J.A. Sanjurjo, C. Rettori, I. Torriani, S.B. Oseroff, J.J. Neumeier, K.J. McClellan, S.W. Cheong and Y. Tokura, Phys. Rev. B 58((17) (1998) 11435.
[26] S.D. Ross, in: *Inorganic Infrared and Raman Spectra* (McGraw-Hill, London, 1972).
[27] M. Couzi and P.V. Huong, Ann. Chim. 9 (1974) 19.
[28] A.E. Lavat and E.J. Baran, Vibrat. Spectrosc. 32 (2003) 167.
[29] T.L. Barr, J. Phys. Chem. 82(16) (1978) 1801.
[30] C.D. Wagner, W.M. Riggs, L.E. Davis and J.F. Moulder, in: *Handbook of X-Ray Photoelectron Spectroscopy* (Perking-Elmer Corporation, Physical Electronics Division. Eden Prairie, Minnesota, 1979).
[31] D. Briggs and M.P. Seah, in: *Practical Surface Analysis*, 2nd ed., Vol. 1, eds. (John Willey & Sons, 1993).
[32] M. Oku and Y. Sato, Appl. Surf. Sci. 55 (1992) 37.
[33] L. Simonot, F. Garin and G. Maire, Appl. Catal. B 11 (1997) 167.
[34] R. Leanza, I. Rossetti, L. Fabbrini, C. Oliva and L. Forni, Appl. Catal. B 28 (2000) 55.
[35] N.A. Merino, B.P. Barbero, P. Eloy and L.E. Cadús, Appl. Surf. Sci. in press.
[36] A.A. Leontiou, A.K. Lavados, T.V. Bakas, T.C. Vaimakis and P.J. Pomonis, Appl. Catal. A 241 (2003) 143.
[37] L. Bedel, A.C. Roger, J. L. Rehspringer, Y. Zimmermann and A. Kiennemann, J. Catal. 235 (2005) 279.
[38] L. Bedel, A.C. Roger, C. Estournes and A. Kiennemann, Catal. Today 85 (2003) 207.
[39] R.D. Shannon, Acta Cryst. A 32 (1976) 751.
[40] J.L.G. Fierro and L.G. Tejuca, Appl. Surf. Sci. 27 (1987) 453.